Focused on New Trends in Fatigue and Fracture

Visual Abstract

Analysis of Low-Cycle Fatigue Behavior of AW2099-T83 Al-Li Alloy

Muhammed J. Adinoyi, Necar Merah, Jafar Albinmousa
Department of Mechanical Engineering, King Fahd University of Petroleum and Minerals, Dhahran, Saudi Arabia
mjadinoyi@gmail.com, http://orcid.org/0000-0001-2345-6789
nesar@kfupm.edu.sa, https://orcid.org/0000-0002-8158-8867
binmousa@kfupm.edu.sa, https://orcid.org/0000-0002-2395-5008

ABSTRACT. Microstructural characteristics, monotonic and strain-controlled cyclic axial behaviors of AW2099-T83 Aluminum-Lithium alloy were investigated. Grain sizes and structures are not uniform in the different orientations studied. High strength and low ductility characterize the tensile behavior of the alloy under static loading. Strain-controlled fatigue testing was conducted at strain amplitudes ranging from 0.3% to 0.7%. Over this range, macro plastic deformation was only observed at 0.7%. Cyclic stress evolution was found to be dependent on both the applied strain amplitude and the number of cycles. Limited strain hardening was observed at low number of cycles, followed by softening, due probably to damage initiation. With low plastic strain, analytical approach was adopted to profile the damaging mechanism for the different applied strain amplitude. Because of the absence of fatigue ductility parameters due to low plasticity, a three-parameter equation was used to correlate fatigue life. Fractured specimens were studied under SEM to characterize the fracture surface and determine the controlling fracture mechanisms. The fractography analysis revealed that fracture at low strain amplitudes was shear controlled while multiple secondary cracks were observed at high strain amplitude. Intergranular failure was found to be the dominant crack propagation mode.

KEYWORDS. Aluminum-lithium; Microstructure; Fatigue behavior; Fatigue damage; Intergranular fracture.

OPEN ACCESS

Citation: Adinoyi, M. J., Merah, N., Albinmousa, J., Analysis of Low-Cycle Fatigue Behavior of AW2099-T83 Al-Li Alloy, Frattura ed Integrità Strutturale, 49 (2019) 487-506.

Received: 02.02.2019
Accepted: 14.04.2019
Published: 01.07.2019

INTRODUCTION

Lightweight alloys such as aluminum (Al) alloys are crucial to the transportation sector, especially the aerospace industry. Aluminum alloys have a long history in the industry because of their low weight and considerable strength [1–4]. Therefore, the history of aircraft material cannot be told without aluminum occupying a prime position. Even with recent effort to replace major parts of the aircraft with composite, Al alloys continue to play a major role in the industry. Thus, the importance of Al alloys in vital components of aircraft has caused an unending research for improved Al alloys.

Aluminum alloyed with lithium (Li) has shown to be a promising material for the aerospace industry due to its high strength-to-weight ratio. Aluminum-lithium (Al-Li) alloy is not an entirely new alloy to the industry. The first major deployment of the alloy in aircraft components was in the 1950s in the form of Al-Li 2020, even though its development started in 1920. Later generations of the alloy which have found application in aircraft components include Al-Li 2090, 2091, 8090 and 8091 [1–4]. The high elastic modulus of Al-Li stands it out compared to traditional aluminum alloys. It is reported that elastic modulus of aluminum metal is increased by 6% while weight is decreased by 3% when it is alloyed with 1% lithium [3–5]. The simultaneous addition of copper and lithium improves the strength of the alloy [6]. However, challenges such as prohibitive cost, poor fatigue performance, low fracture toughness, poor corrosion resistance and high anisotropic behavior constrained the wide deployment of Al-Li in the aircraft industry [1,2,7,8]. Perhaps, poor fatigue performance is the larger reason that sundry works on different generations of the alloys were focused on fatigue crack behavior [9–15].

While there is growing research interest in the tensile behavior of the Al-Li, fatigue studies of the alloy are scarce in the open literature. Srivatsan and Coyne [8] studied the cyclic deformation behavior of both Al-Li-Cu and Al-Li-Mn alloys and showed that while the former hardened to failure due to dislocation-precipitates interaction, the latter softened to failure at all strain amplitudes and possessed poor fatigue property. Blankenship et al. [16] reported that direct-chill cast and rolled X2095 Al-Li showed immediate cyclic softening accompanied by a plateau region with homogeneous distribution of strain over its microstructure. Liu and Wang [17] performed strain-controlled fatigue testing on heat treated and equal channel angular pressing (ECAP) 8090 Al-Li and found that the fatigue behavior of the alloys differed due to different processing parameters which imposed varying fracture mode and deformation.

The third generation of Al-Li alloy has, in recent times, attracted renewed research interest because of its comparably high strength [18–23]. This generation of Al-Li alloy contains less than 2% Li and has been reported to exhibit better corrosion resistance, fatigue crack growth resistance, amenability to various welding technology and higher mechanical strength and toughness [13,24–27]. It was anticipated that the new generation of Al-Li alloy may find its presence in aircraft components such as the fuselage skin, wing, doors, windows, etc. [2,3]. AW2099-T83 is one of the third generation Al-Li alloys whose tensile and microstructural characteristics have, in recent years, gained renewed interest [21,22]. However, like its counterparts, very limited information about its fatigue behavior is available in the open literature. Adinoyi et al. [28] studied the shear strain-controlled fatigue behavior of AW2099-T83 and concluded that the alloy has very low plasticity and that macroscopic plastic strains evolved only at high strain amplitudes. The authors further showed that cracking behavior of the alloy is dependent on applied strain amplitude.

The present work intends to study the microstructural characteristics in different orientations, monotonic tensile and axial strain-controlled fatigue behavior of Al-Li AW2099-T83. The study will determine the monotonic and cyclic properties of the material under tensile loading conditions. These will be used to estimate the fatigue life of the material. Fractured specimens will be directly observed under optical and Scanning Electron Microscope (SEM) to determine the controlling fracture mechanisms.

MATERIAL AND EXPERIMENTATIONS

The Al-Li used in the present study is an extruded AW2099-T83/SHP, acquired from Smiths Metal Centres, Ltd, Bedfordshire, UK. The chemical composition of the material is illustrated in Tab. 1. Microstructure analysis was conducted on specimens taken from the transverse orientation (diameter of the bar) and along its length (extrusion direction) as shown in Fig. 1. E1 and E3 are notations to represent sample taken from the edge and the center of the extrusion orientation. While E2 is the sample from midway between E1 and E3. Likewise, T1, T2 and T3 denote similar locations in the transverse orientation. Samples were ground, polished with diamond paste and etched in sodium hydroxide solution before microscopic observation. Tensile test specimens (Fig. 2(a)) were machined parallel to the extrusion direction, with a gauge length of 25.0 mm and a gauge diameter of 6.0 mm. Tensile tests were conducted at a crosshead speed of 2 mm/min on Instron 5569 tensile test machine, according to ASTM E8-08 Standard [29]. Extensometer with 12.5 mm gauge was used to measure strains up 1% after which it was removed and the test was switched to displacement-controlled condition. Five tensile tests were performed and the resulting force and strain data, automatically recorded in the computer during the test, were analyzed to determine the tensile properties of the alloy.

The strain-controlled tension-compression tests were conducted as per ASTM E606-12 Standard [30] on smooth solid specimens (Fig. 2(b)) using Instron servo-hydraulic test frame with a load capacity of 100 kN. The solid specimens were prepared on a CNC machine with aerospace certified coolant. Gauge sections were machined in one pass for a uniform profile. This was followed by three-stage polishing with aluminium oxide abrasive belts of grades P240 (59 μm), P400 (39 μm) and P800 (22 μm), respectively. Alignment cells were used on test fixture to minimize off-axis load and incident of

buckling. The extensometer used has a gauge length of 11 mm. Following testing, fractographic analysis was conducted on fractured specimens of selected strain amplitudes under JOEL JSM6610 Scanning Electron Microscope (SEM).

Element	Al	Cu	Fe	Li	Mg	Mn	Si	Ti	Zn	Zr
wt%	94	2.7	0.02	1.8	0.29	0.3	0.02	0.03	0.7	0.1

Table 1: Material chemical composition.

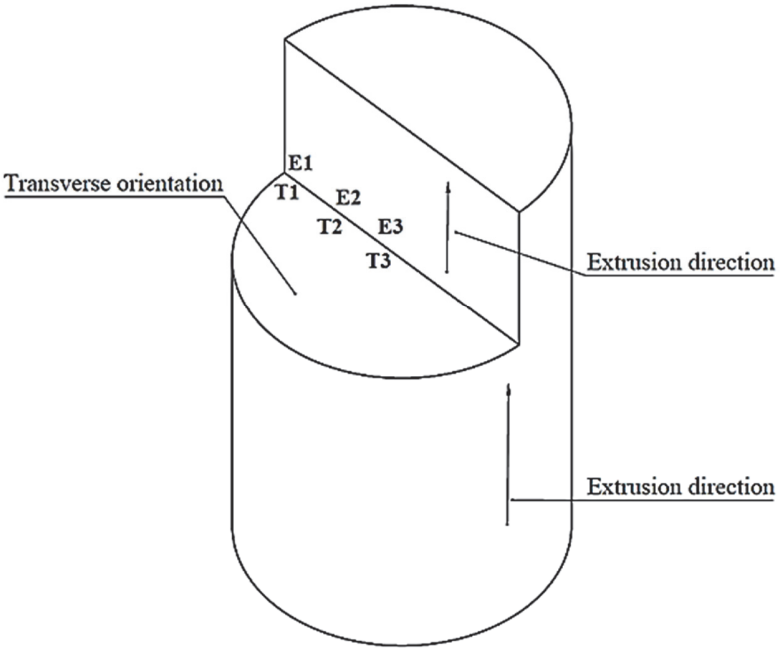

Figure 1: Illustration of locations of sample for metallography analysis.

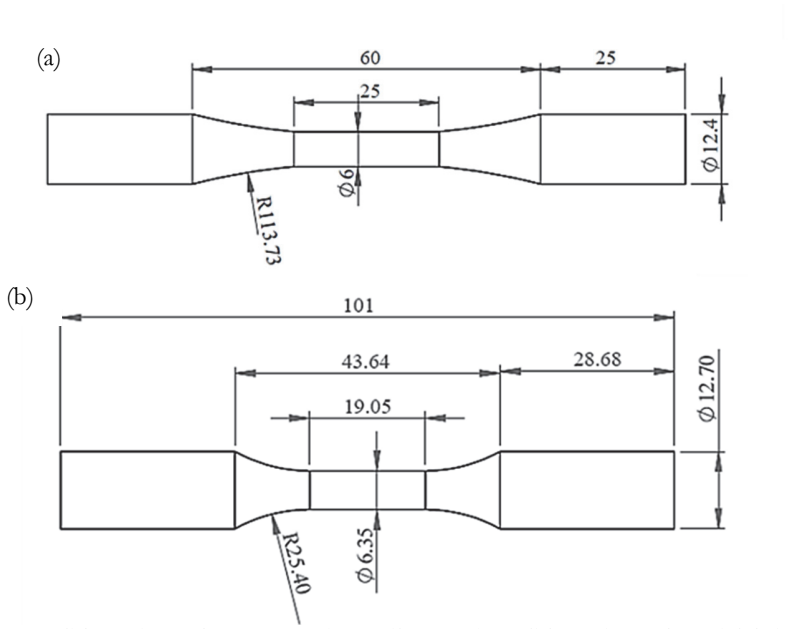

Figure 2: (a) Solid specimen for monotonic tensile test, (b) Solid specimen for axial fatigue test.

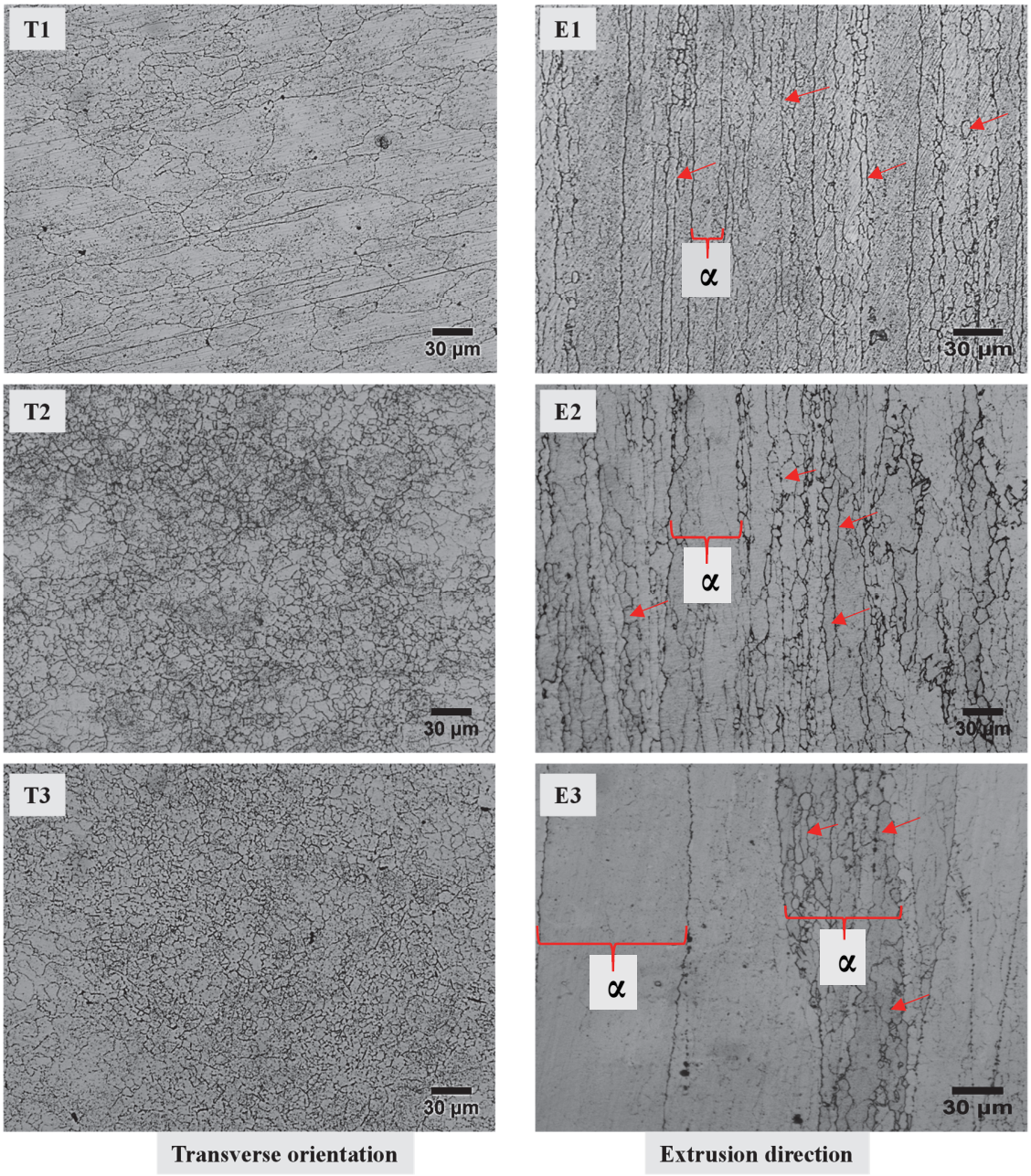

Figure 3: Optical metallographs of the AW2099-T83 alloy at different locations for transverse and extrusion directions.

Results and Discussion

Microstructure

Fig. 3 shows the microstructure of AW2099-T83 in the various locations in the transverse (T1, T2, T3) and extrusion directions (E1, E2, E3) analyzed. The structure in the transverse orientation at location T1 is composed of clusters of small grains, measuring about 10 µm, intermingling with large grains of approximately 80 µm. The small grains resulted from recrystallization after solution heat treatment, while the large grains are unrecrystallized structures [21,24]. Comparable microstructures were reported for materials of similar type and were attributed to dynamic recovery and the presence of Al_3Zr [31,32]. It is noted that grains become smaller towards the radius of the billet as can be seen in the micrographs representing T2 and T3 locations and these measure approximately 5-8 µm. However, in the direction of extrusion, elongated primary grains donated by α can be seen in the micrographs marked E1, E2 and E3 in Fig. 3. Within

the primary grains are subgrains, indicated by arrows, which either are aligned parallel to the primary grains or are equiaxial. The subgrains are the product of recrystallization process as previously stated. It can be observed that primary grains are wider in E3 than E2. The sizes of the grains vary between 6 and 13 μm in thickness. As reported by Lin et al [22], elongated grain is due to severe deformation taking place in the surface layer during hot extrusion. Al-Li alloys have been reported in several studies as possessing varied grain structure and size in different orientations [21,22,31,33]. The existence of inhomogeneous grain sizes and structures in different orientation is a precursor to anisotropy in the behavior of the alloy.

Static Tensile Behavior

The characteristic engineering stress-strain curve for the alloy is presented in Fig. 4. It shows that AW2099-T83 exhibits a deformation behavior nearly similar to that of an elastic, perfectly plastic material with a very limited amount of post yielding strain work hardening. Even though post yield hardening is small, data from the plastic region of the curve is fitted to Eq. (1) to estimate the hardening behavior represented by the strength coefficient K and hardening exponent n. These values and other tensile mechanical properties are illustrated in Tab. 2 along with their standard deviations.

$$\sigma = K\varepsilon^{n} \tag{1}$$

It can be observed that the tensile strength is comparable to similar material [18,31] but higher than several other types of Al-Li alloys [3,7,19,24,34] reported in the literature. It has been shown that increase in the Cu and Li contents of the alloy promotes the formation of strengthening precipitates such as Al_2CuLi and Al_2Cu phases which increase the alloy's strength [13,24,35]. Aging condition, homogenization heat treatment, orientation of testing and precipitate phases have been identified as vital factors which influence the alloy's tensile properties [5,18,21,22,31]. It is worth mentioning that in spite of the high number of researches on the tensile property of the alloy, the characteristic stress-strain curve is rarely reported. It is noticed that the alloy exhibits high strength, while it possesses low ductility. Similar results was recorded by Zheng et al. [36] for 2060 Al-Li. The low ductility can be regarded as tradeoff for the high tensile strength. However, such a balance is not unusual for structural alloys. The observable strain in tensile strength will be used as the basis for choosing the applied strains in cyclic test.

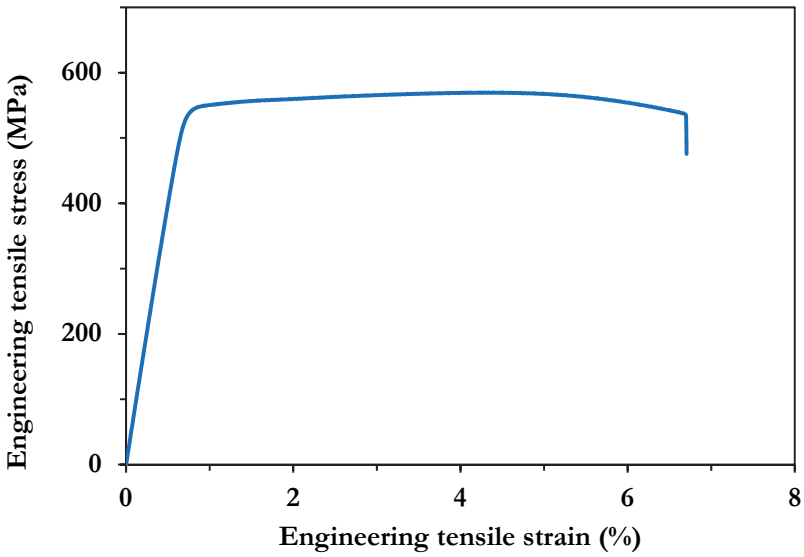

Figure 4: Engineering stress-strain curve for the investigated AW-2099-T83.

Low Cycle Fatigue Behavior of AW2099-T83

Hysteresis loops

Representative hysteresis loops at second cycles, half-life cycles and near failure are shown in Fig. 5, for each of the investigated strain amplitudes (ε_a). The second cycle is chosen, being the first complete loop, while at half-life cycle is considered to have a stabilized loop. The post half-life loop is representing a near-failure cycle, which may be significantly different from events at earlier cycles. This selection is expected to illustrate the cyclic trend and loop evolution through the fatigue life of the material, for each strain amplitude. It can be seen from Fig. 5 that the alloy exhibits no macroscopic plastic

strain for the applied ε_a less than 0.7%. Thus, the deformation of the alloy over the strain amplitude of 0.3%-0.6% is elastic; indicating that the total strain was recovered in each cycle. Similar behavior was recorded by Adinoyi et al. [28] for the same material under shear fatigue at strain amplitudes less than 1.0%. The implication of this characteristic evolution of the hysteresis loop is that energy-based fatigue models [37,38] dependent on plastic strain may be inapplicable to the present alloy, in this strain range. It is also noticed that for this range of applied ε_a, cyclic hardening/softening behavior is insignificant, as the loops superimpose on each other, irrespective of the number of cycles. However, at the ε_a =0.7%, a plastic strain of about 0.1% at half-life was measured. In addition, there is a slight increase in plastic strain as the number of cycles increases from the second cycle through the half-life cycle. The plastic strain shown by the present alloy at ε_a = 0.7% is still small compared to most other alloys. In general, two important factors are liable for limited cyclic plastic deformation in alloys; high mechanical strength resulting from microstructure or strain amplitude too low to activate plastic deformation. The strengthening mechanism of the present alloy, as mentioned in section 3.2, creates many precipitates that inhibit plastic deformation. Such an alloy with high mechanical strength and low ductility resists applied strain in an elastic manner resulting in very slim hysteresis loops [39].

Engineering Tensile Property	Value
Tensile strength (MPa), U_{ts}	567 ± 10.11
0.2% Yield stress (MPa)	549 ± 9.26
Elastic Modulus (GPa), E	80 ± 0.84
Strain hardening coefficient, K (MPa)	680 ± 15.76
Strain hardening exponent, n	0.0437 ± 0.01
Reduction in area (%)	8.0 ± 0.02
Elongation (%)	2.5 ± 0.22
Fracture stress (MPa)	530 ± 4.95
Fracture strain (%)	6.58 ± 0.7

Table 2: Average tensile mechanical property for AW2099-T83.

Cyclic Stress Evolution

The cyclic stress evolution, illustrated in Fig. 6(a), shows that the maximum and minimum stresses vary with the number of cycles for all the applied strain amplitudes. The point at which stress changes with respect to cycle is different for each ε_a, indicating that the maximum value of the cyclic stress is influenced by the applied strain amplitude.

At ε_a =0.7%, maximum stress slightly increases until the 5th cycle, followed by stress stabilization before dropping to the initial value. A similar trend is observed for the minimum stress with the latter showing lower absolute values. The stress increment during hardening at 0.7% is about 25 MPa. A similar behavior is observed at ε_a = 0.6% with higher initial cyclic hardening of about 40 MPa. After about 100 cycles of stress stabilization, the alloy cyclically softened to failure. At applied strain amplitudes of 0.3 to 0.5%, cyclic hardening resulting in a rise of stress of about 10 to 40 MPa is observed until failure.

Cyclic hardening at low strain amplitude for the alloy may be explained by the change in the dislocation density of the material due to slip deformation [40]. When an alloy is cyclically strained, slips happen, and dislocation gradually builds up. The rise in dislocation density however restricts dislocation mobility [40]. This restriction manifests in the form of stress increment or cyclic hardening. Cyclic hardening can also be due to dislocation-dislocation interaction or dislocation pile-up [41]. Srivatsan and Coyne [8] have reported that Al-Li-Cu alloys generally softened to failure under plastic strain amplitudes ranging between 0.02% and 1.8%. The authors [8] explained that once precipitates are cut, particles offer less resistance to dislocation movement in the active slip plane and local work hardening capacity are reduced resulting to cyclic softening. It has already been recognized by Liu and Wang [17] that Al-Li processed by ECAP may soften to various degrees under cyclic loading. The rate of softening depends strongly on the initial structure and loading conditions and may vary in a wide range, because the microstructure is far from equiaxial and the dislocation density is high. Likewise, the microstructure for the present alloy, as observed in Fig. 3, is far from being equiaxial. The orientation of a particular structure and associated strengthening precipitate with loading cycle would determine the behaviour at that instance. Elongated structures with accompanying long grain boundaries have weak resistance to loading and this might appear as softening. On the other hand, short grain boundaries resulting from small grain size create tortuous path and offer resistance that may appears as cyclic hardening.

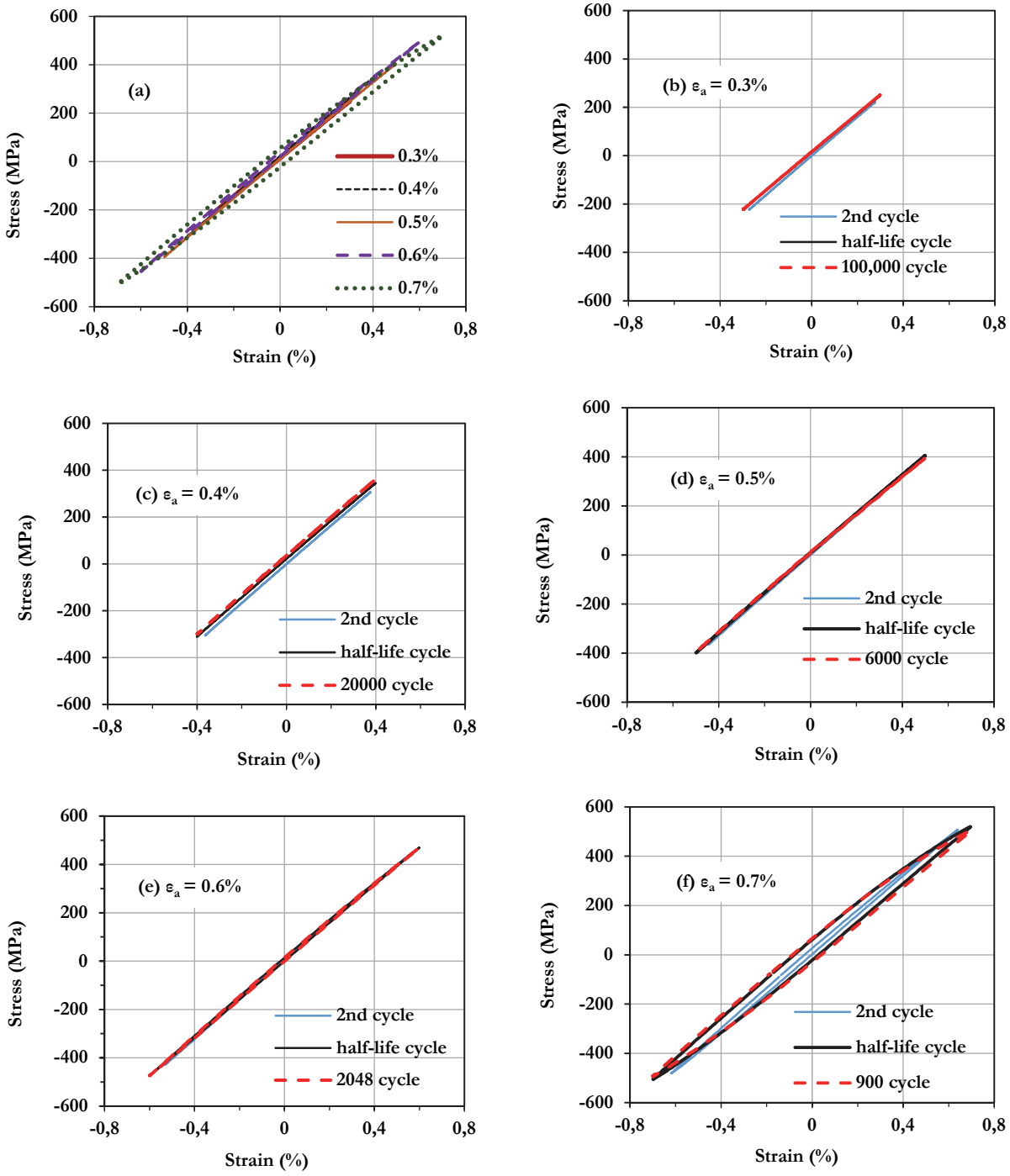

Figure 1: Representative hysteresis loop evolution for all investigated strain amplitudes; (a) stabilized cycles; (b)-(f) for selected cycles.

Fig. 6(b) displays the mean stress (ε_m) evolution with the number of cycles for the alloy. For a major part of the cycling, negative mean stress evolved at applied strain amplitudes of 0.3% to 0.6%. However, there is a tendency for the mean stress to rise abruptly with increasing number of cycles at lower applied strain amplitudes. In contrast, strain amplitude of 0.7% produces tensile mean stress of about 10 MPa for the entire fatigue life. Mean stress development indicates the asymmetry of cyclic stress. It is clear from the illustrations in Fig. 6(b) that mean stress evolution for the present alloy is dependent on both applied strain amplitude and number of cycles. This may be due to its microstructure and strengthening mechanism. The evolution of tensile mean stress with the number of cycles for the alloy may suggest that, the density of dislocation

increases, resulting in dislocations-dislocation interaction [8]. This interaction will result in cyclic hardening, translating to positive mean stress. Thus, the abrupt rise in the mean stress at higher number of cycles can be attributed to increase in dislocation density. The ε_m behavior for the alloy can then be summarized as follows: for ε_a less than 0.6%, the ε_m is compressive but rises to become tensile if the fatigue life exceeds three thousand cycles or when applied strain amplitude is above 0.6%.

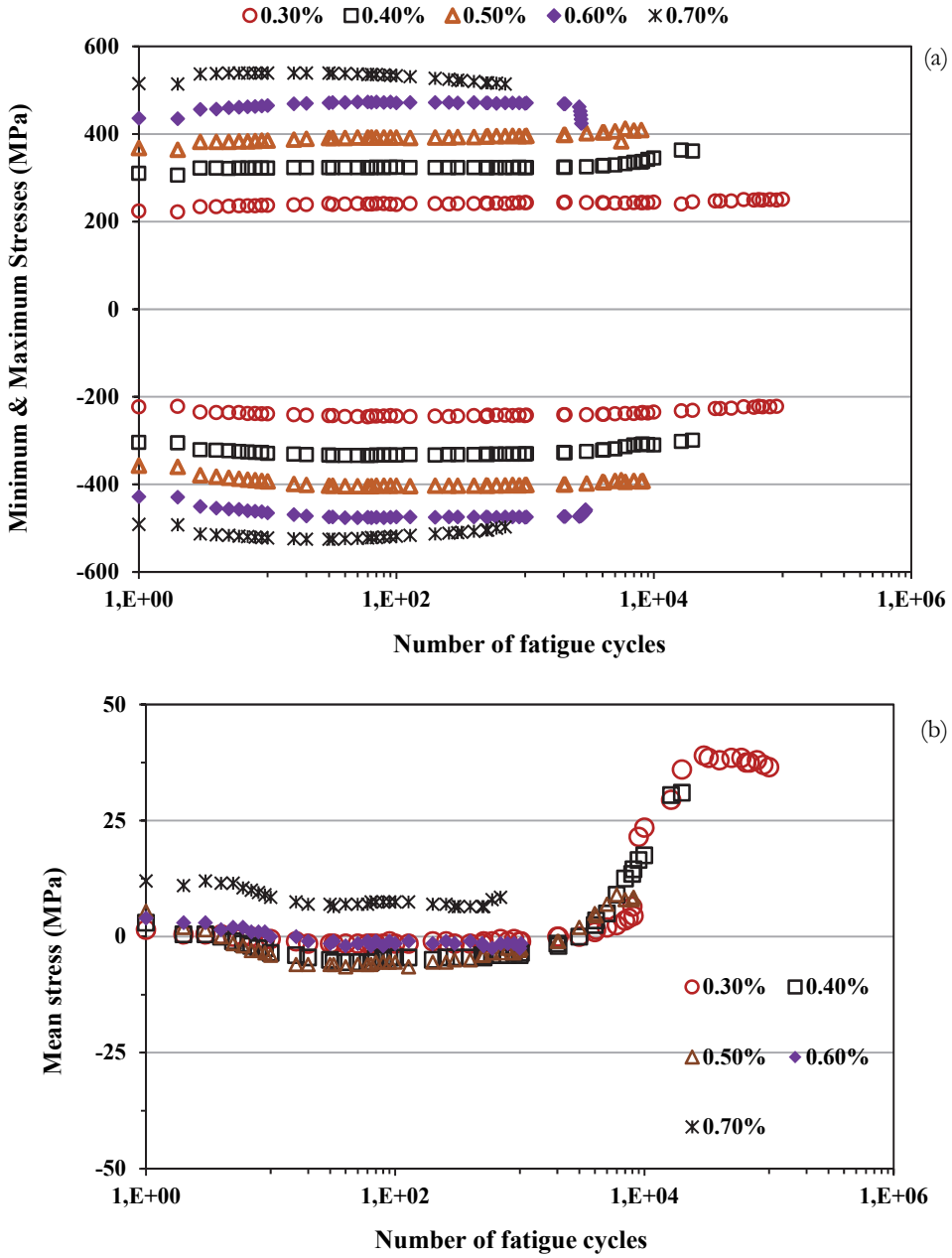

Figure 6: Variation of (a) the maximum and minimum stresses with the number of fatigue cycles, (b) Mean stress with number of fatigue cycles.

DAMAGE ASSESSMENT THROUGH RESIDUAL STIFFNESS AND ESTIMATED STRAIN COMPONENTS

Plastic strain is an important parameter for the assessment of fatigue damage in fatigue loading. However, the current alloy exhibits no discernible plastic deformation for the majority of the strain amplitudes investigated. Thus, it is devised to evaluate damage through the trend analysis of the residual stiffness, E_s. The residual stiffness is analogous

to elasticity. However, elasticity is associated with previously unloaded sample; hence, the term residual is being considered. The residual stiffness is estimated by taking the slope of the unloading reversal for all sample tested as illustrated with half loop in Fig 7. Fig. 8 shows the trend for residual stiffness with percentage cycle for every 10% of the total loop sampled per strain amplitude. Each test at all strain amplitudes was replicated. Thus, the notations 1 and 2 are for the first run and its replicate, respectively. The observed trend is that there is no significant change in the stiffness with increase cycle and strain amplitude. The value of the stiffness fluctuates around 77-80 GPa which is in close agreement to the stiffness in uniaxial tensile. However, there is an abrupt drop in the stiffness at 0.4% and 0.6%. This signifies a significant damage in the specimens as typified by distortion in the hystereses loops shown in Fig. 9. The half-life loops are also plotted for comparison. It can be seen that the more rapid the drop in the stiffness, the more distorted the loop is. Hence, damage can be assessed through stiffness.

In addition, an assumption is made by estimating strain components from the stiffness by the application of Eqns. (2), (3) and (4), where ε_t, ε_e and ε_p are the total, elastic and plastic strains, respectively. Maximum stress from portion of the loop that was analyzed for stiffness calculation is used to represent σ_a in order to calculate for the elastic strain according to Eq. (3). Hence, plastic strain is estimated according to the relation in Eq. (4)

$$\varepsilon_t = \varepsilon_e + \varepsilon_p \tag{2}$$

$$\varepsilon_e = \frac{\sigma_a}{E_s} \tag{3}$$

$$\varepsilon_p = \varepsilon_t - \varepsilon_e \tag{4}$$

The trend in the estimated plastic strain with loop percentage is shown in Fig. 10. The plots are separated for strain amplitudes (0.3-0.6%) which show no plastic deformation in the hysteresis loop and those (0.7%) that exhibit plastic strain as previously observed in Fig. 5. The following deduction can be made: regardless of applied strain amplitude, the initial ten cycles for the alloy will exhibit tensile plastic deformation. Beyond the 10% cycles, the plasticity evolves into a compressive strain in the strain amplitudes (0.3%-0.6%) which shows no observable plastic strain. However, strain amplitude at 0.7% where visible plastic strain is present maintains a tensile plastic strain that rapidly rises in value toward the end of the cycle. Thus, there is a trend for the likely underlying mechanism for the damage in the alloy. It shows that compressive strain is the damaging strain in the alloy at strain amplitude below 0.7%, while tensile strain is the dominant effect at strain amplitude equal or greater than 0.7%. The trend observed correlate with that shown by the mean stress illustrated in Fig. 6(b).

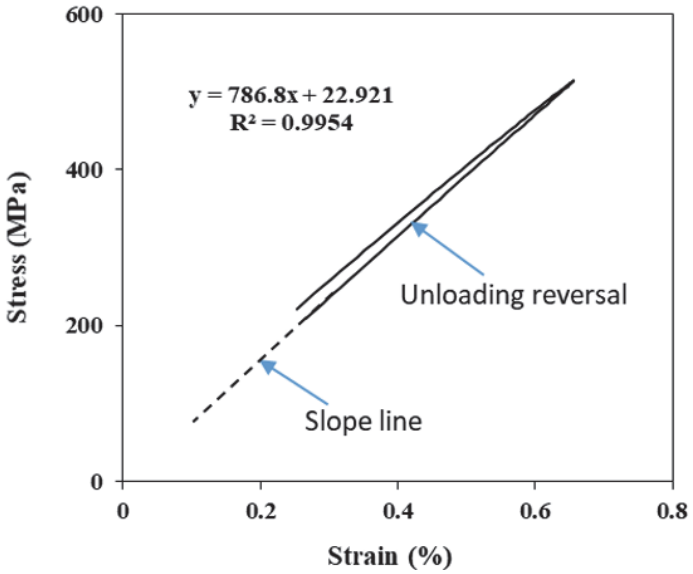

Figure 7: Illustration for the estimation of residual stiffness.

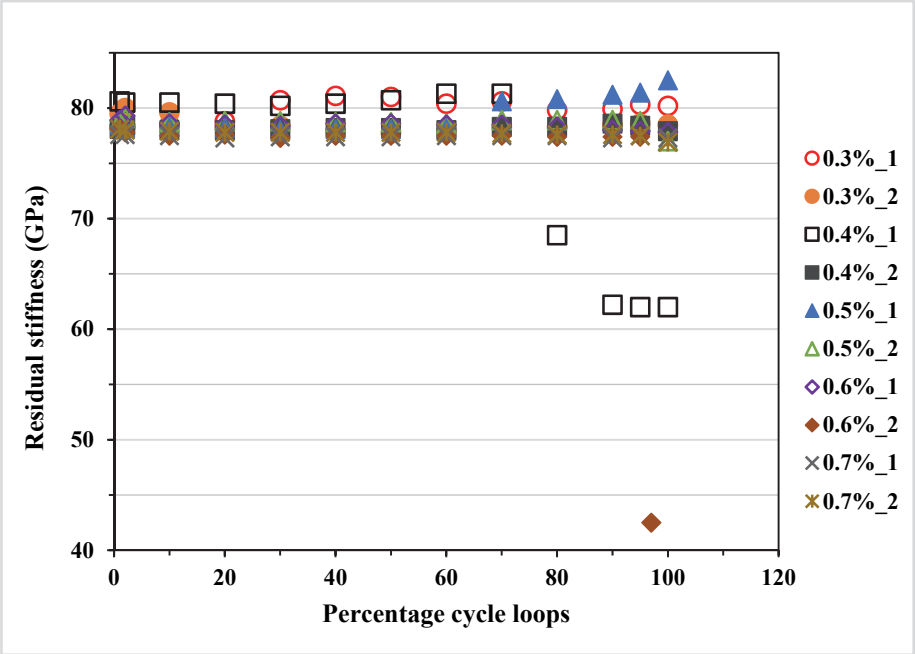

Figure 8: Residual stiffness vs. percentage sampled hysteresis loops.

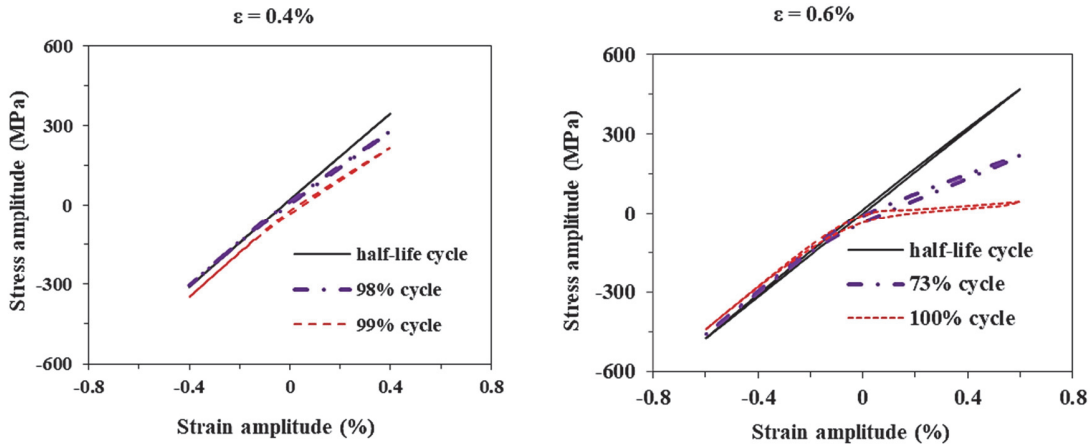

Figure 9: Illustration of Damaged Loops Resulting in Reduced Stiffness.

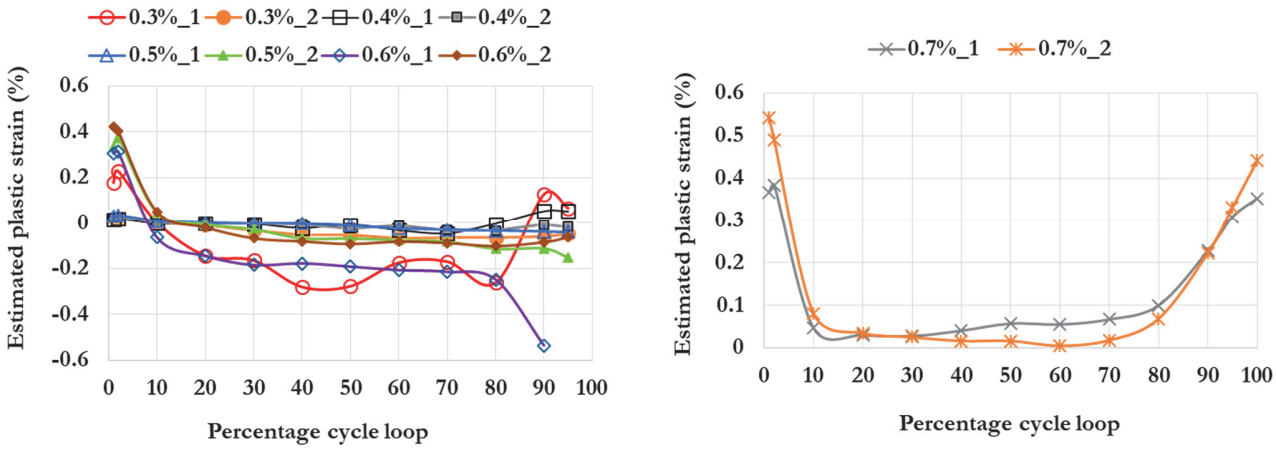

Figure 10: Estimated plastic strain versus percentage of cycle loops.

Strain-life correlation

The correlation between strain amplitude and fatigue life in strain-controlled tests is often represented by a strain-life curve described usually by the Coffin-Manson equation:

$$\varepsilon_a = \frac{\sigma_f^{'}}{E}\left(2N_f\right)^b + \varepsilon_f^{'}\left(2N_f\right)^c . \tag{5}$$

where $\sigma_f^{'}, \varepsilon_f^{'}$, b and c are respectively, the fatigue strength coefficient, fatigue ductility coefficient, fatigue strength exponent and fatigue ductility exponent. Summary of experimental strain amplitudes, stress responses and fatigue life at half–life cycles are presented in Tab. 3. Regression analysis was performed on the data, as illustrated by the curve in Fig. 11, to obtain the material fatigue properties in Eq. (5). Because of the absence of plastic deformation, only the parameters $\sigma_f^{'}$. and b. can be determined. Strain-controlled fatigue experimental data for Al-Li alloys is scarce in open literature. Common aerospace grade alloys with which AW-2099-T83 can be compared are shown in Tab. 4. It is found that the magnitudes of $\sigma_f^{'}$ and $|b|$ obtained in the present study are higher. The fatigue strength coefficient is approximately two to four times higher than those reported for conventional aluminum alloys. High fatigue strength coefficient is an indication of good fatiigue properties especially in the high cycle fatigue (HCF) regime. However, it should be noted that with higher strain amplitude that would initiate plastic strain, the value of $\sigma_f^{'}$ decreases and thus lowering the HCF performance. High fatigue strength coefficient for Al-Li is as a result of high monotonic strength rather than good fatigue resistance [37]. Similarly, the stress-life evolution is compared to recently published work for other types of Al-Li alloys [7] as shown in Fig. 12. Stress-life profile for the three alloys is similar for stress amplitudes between 220 and 340 MPa. The trends in the curves indicate that fatigue limit is likely to be achieved for Al-Li alloys for stress amplitudes less than 200 MPa. Due to its higher tensile strength, the capacity of the present alloy to accommodate higher cyclic stress is noticeable. However, taking into account that strengthening phases and heat treatments are different, such a comparison is influenced by these factors. It is also worth mentioning that the stress amplitude used in Fig. 12, for AW2099-T83, is that obtained at half-life.

The strain-life curves for completely reversed loading are shown in Fig. 13. Due to the observed low plasticity behavior of AW2099-T83 over the range of strain amplitude studied, both total and elastic strain curves are superimposed on each other. Alloys with low plasticity usually exhibit high strength coefficient $\left(\sigma_f^{'}\right)$ but low ductility coefficient $\left(\varepsilon_f^{'}\right)$ causing the fatigue behavior to be dominated by elastic behavior, as was observed in the hysteresis loops in Fig. 5. Since the plastic strain data is insufficient to obtain a reliable curve fit for ductility exponent, *c*, the strain-life equation for AW2099-T83 is merely the Basquin equation. Therefore, the strain-life equation for AW2099-T83/SHP is expressed in Eq. (6).

$$\varepsilon_a = \frac{1650.30}{80300}\left(2N_f\right)^{-0.151} \tag{6}$$

where ε_a is the applied strain amplitude and N_f is the fatigue life.

Alternatively, because of the low plastic deformation, it is assumed that Coffin-Manson equation or any of its component relation is insufficient as life correlation for the present alloy. Hence a three-parameter equation, first proposed by Manson [42], is used to characterize strain-life behavior. The expression for his equation is shown in Eq. (7).

$$\left(\varepsilon_a - \varepsilon_o\right)^{\mu} N_f = C \tag{7}$$

where $\varepsilon_o, \mu \, and \, C$ are fitting constants that can be considered as unique material properties. $\varepsilon_{o,}$ can be viewed as the strain endurance limit [42]. The fitting constants were found through regression analysis. The fatigue curve based on this equation is illustrated in Fig. 14 and the corresponding equation, for the present alloy, is expressed as:

$$\left(\varepsilon_a - 0.000289\right)^{5.66} N_f = 4.7\times10^{-10} \tag{8}$$

Although both the Basquin curve and three-parameter curve are similar, however, the latter curve shows a slightly better correlation for the experimental data.

Spec. ID	d (mm)	ε_a (%)	σ_{max} (MPa)	σ_{min} (MPa)	σ_a (MPa)	σ_m (MPa)	ε_e (%)	ε_p (%)	N_f (Cycle)
63448C	6.37	0.3	249.63	-223.12	236.38	13.26	0.3	0	100,000 (stopped)
63449C	6.37	0.3	281.78	-206.33	244.06	37.73	0.3	0	156375
63446C	6.36	0.4	344.75	-309.97	327.36	18.39	0.4	0	23066
63447C	6.37	0.4	320.03	-313.24	316.64	3.39	0.4	0	37215
63444C	6.36	0.5	404.14	-394.06	399.1	5.04	0.5	0	8925
63445C	6.36	0.5	404.92	-398.82	401.87	3.05	0.5	0	6875
63450C	6.36	0.6	493.4	-453.25	473.33	20.08	0.6	0	1816
63452C	6.36	0.6	469.36	-473.54	471.45	-2.09	0.6	0	2966
63451C	6.37	0.7	520.21	-506.73	513.47	6.74	0.6	0.1	785
63453C	6.36	0.7	519.37	-505.12	512.25	7.13	0.6	0.1	929

Table 3: Axial strain-controlled fatigue parameters and results.

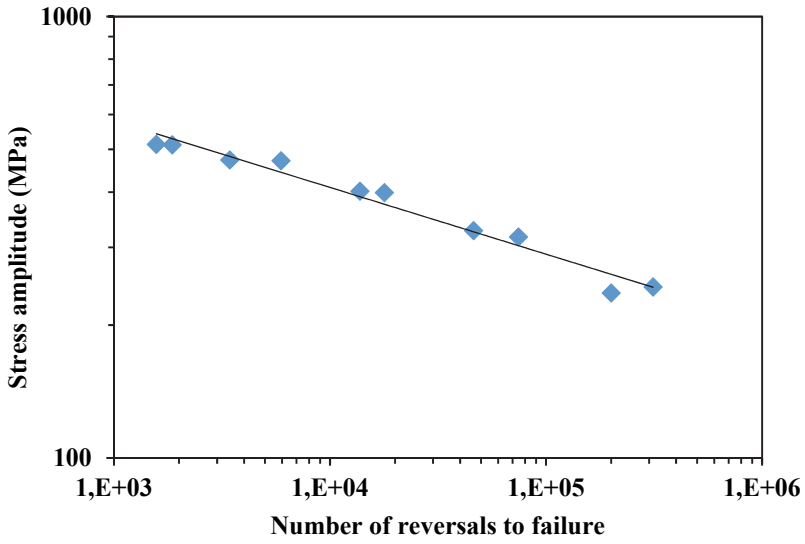

Figure 11: Regression curve to evaluate fatigue properties.

Al alloys	σ_f' (MPa)	b	ε_f'	c	ref
AW2099-T83	1650.3	-0.151	-	-	Present work
2024-T3	850	-0.086	0.22	-0.462	[43]
6060-T6	376.5	-0.084	0.157	-0.537	[44]
6082-T6	486.8	-0.07	0.209	-0.593	[44]

Table 4: Comparison of fatigue constants of the present alloy with conventional Al alloys.

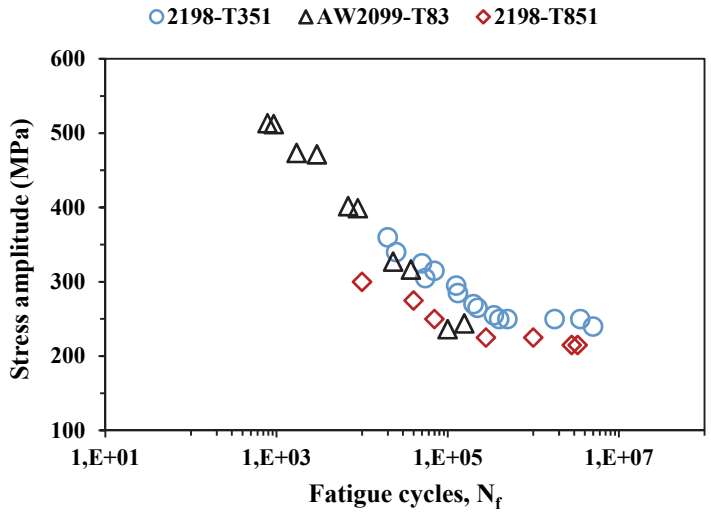

Figure 12: Comparison of the Stress-Life curve with other Al-Li alloy.

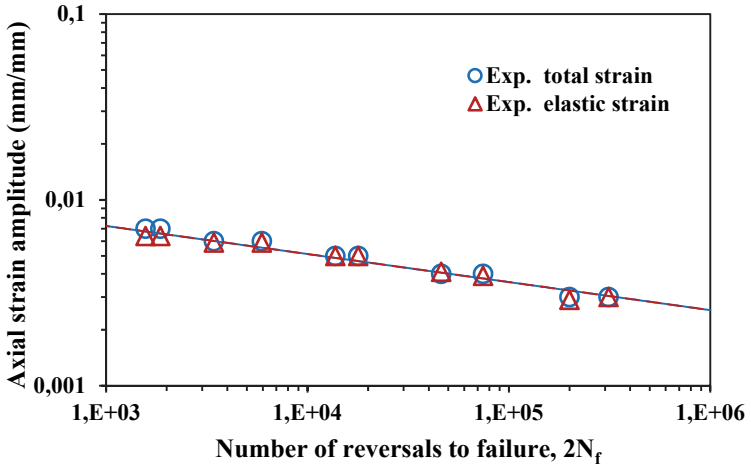

Figure 13: Strain-life curve for AW2099-T83 alloy.

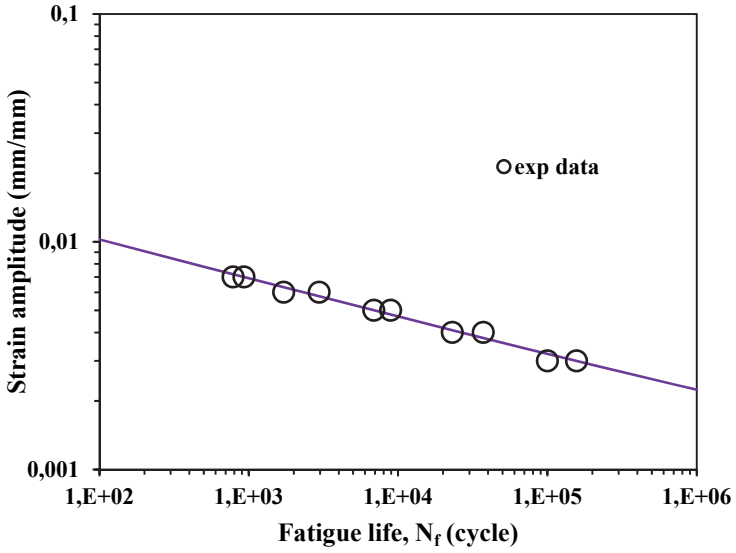

Figure 14: Strain-life curve bases on three-parameter.

FRACTOGRAPHY

SEM of Fractured Surfaces

The fracture surfaces of specimens for selected strain amplitudes are shown in Fig. 15. The SEM fractographs for AW2099-T83 tested at ε_a = 0.3% are presented in Fig. 15(a). The overall fracture happened on a plane of maximum shear suggesting that the load causing the final fracture is shear in nature. As can be seen in Fig. 15a(i), the fractured surface exhibits two separate areas: a fibrous section and a fairly smooth area with ridges. Higher magnifications of the different zones of fractured surface are illustrated in Fig. 15a (ii-iv). The fibrous area indicates that the crack initiated from the edge of the smooth area (Fig. 15a(ii)). Final fracture zones usually show fibrous appearance [40,45]. The transition zone from slow crack propagation to rapid crack growth area (Fig. 15a(iii)) suggests that a shear deformation occurred during this transition. The ridges on the smooth region are perhaps beach marks indicating crack arrests. Fig. 15a(iv) is a higher magnification micrograph showing cleavage fracture.

SEM micrographs for the specimen tested at ε_a =0.5% are shown in Fig. 15(b). It can be seen that, the overall fracture surface exhibits a wedge or bevel shape. A slow crack propagation region and crack initiation areas can be seen in Figs. 15b(i) and 15b(ii). The presence of secondary crack in this region can be seen as illustrated in Fig. 15(b)(iii). The secondary crack appears to follow a grain boundary. The final fracture area, shown in Fig. 15b(iv), presents a texture that is characteristics of a semi-ductile fracture.

The fractographs of Fig. 15(c) are those of fractured specimen under ε_a = 0.7%. The surface consists of a flat region (marked A) and a slant final fractured surface (marked B). Similar fracture has been reported by Alexopoulos et al. [7] for 2198 Al-Li. The multiplication of secondary cracks, due to higher ε_a is clearly visible in Fig. 15(c)(iii). Evidence of crack branching can also be observed on the same illustration. The fracture region of Fig. 15(c)(iv) is similar to that obtained at lower strain amplitudes. It is noted that cracks propagated along grain boundaries as evident from Figs. 15b(iii) and 15c(iii). Elongated grains as identified for the microstructure (Fig. 3) are susceptible to fatigue cracking along grain boundaries.

Analysis of Secondary Crack Behavior

For a further analysis of secondary crack characteristics, optical micrographs of observed cracking features on the fractured surface and on the gage section close to fracture point for specimen tested at a strain amplitude of 0.6% is presented in Fig 16, with the red arrow indicating loading axis. The surfaces were etched in a solution of sodium hydroxide. In the micrograph on the left side of Fig. 16(a), two adjacent secondary cracks are seen to have propagated on the fractured surface of the specimen. The thinner crack advanced faster than the larger one. Both cracks initiated from the surface of the specimen. A close-up look on a section of the thinner, but longer crack is shown on the right side micrograph of Fig. 16(a). It can be observed that the crack meandered through several grain and grain boundaries. Therefore, the cracking is mainly intergranular and partially transgranular. Intergranular fracture was also reported by Wang and Liu [17] for heat-treated 8090 Al-Li. Comparing the fractured surface with the microstructure shown in Fig. 3, it can be inferred that crack growth occurred on the location T1 in the transverse orientation. The transverse orientation is the plane of loading in the cyclic axial fatigue. This location possesses the large, unrecrystallized grains which have been recognized to reduce Al-Li resistance to crack growth [24,32]. The susceptibility of large and elongated grains of A356 Aluminum alloys to cracking have been reported by Mo et al [46].

Fig. 16(b) shows secondary cracks observed under the microscope on the outer surfaces near to the specimen fracture zone. It can be seen that cracks propagated along the grain boundaries, whether in the region of the elongated grains or the smaller subgrains. For a comparison between microstructure over which cracks are present to the microstructure in Fig. 3, it can be observed that grain boundaries in the tested specimen have become wider, signifying that fracture was preceded by grain boundary separation. Elongated grains in the AW2099-T83 are hence weak regions for fatigue cracks to exploit.

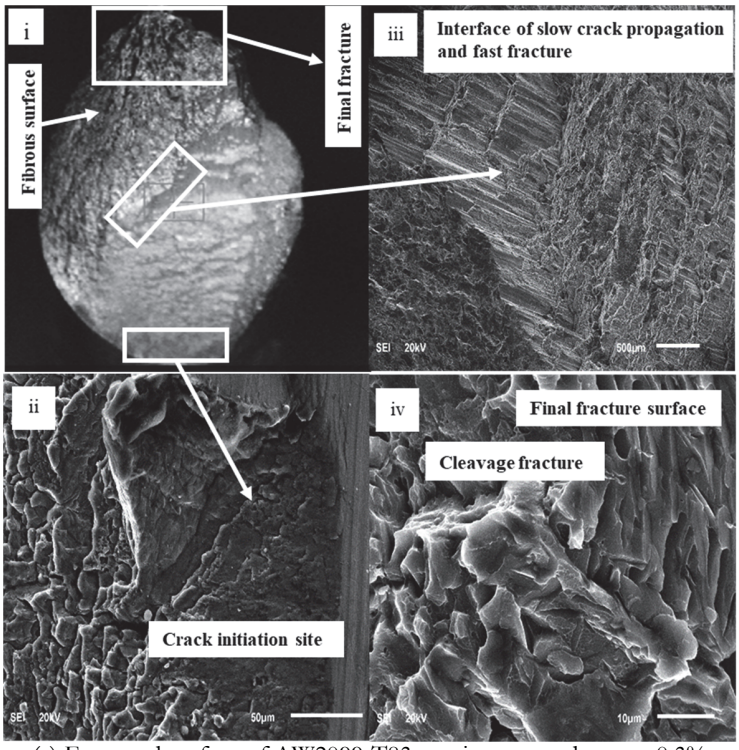

(a) Fractured surface of AW2099-T83 specimen tested at ε_a = 0.3%.

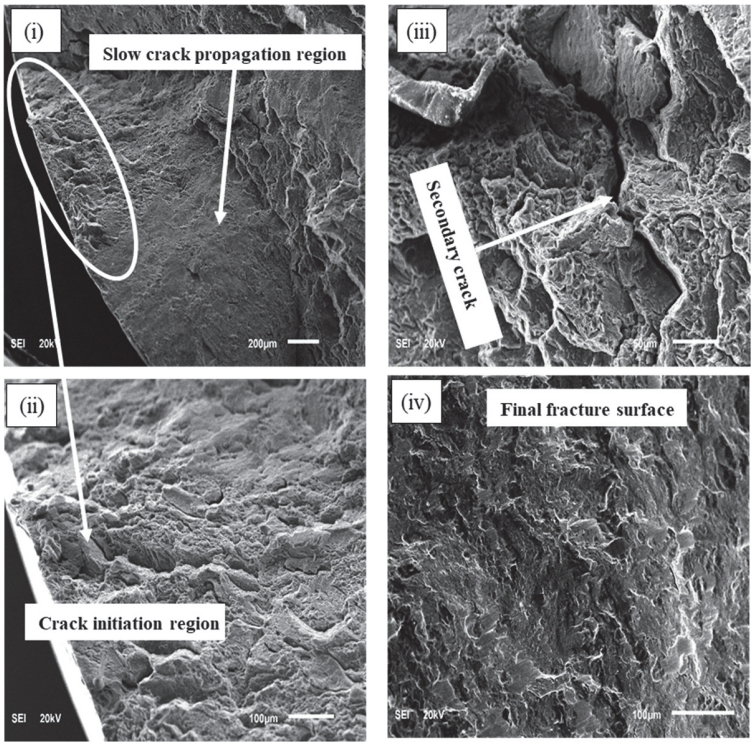

(b) Fractured surface of AW2099-T83 specimen tested at ε_a = 0.5%.

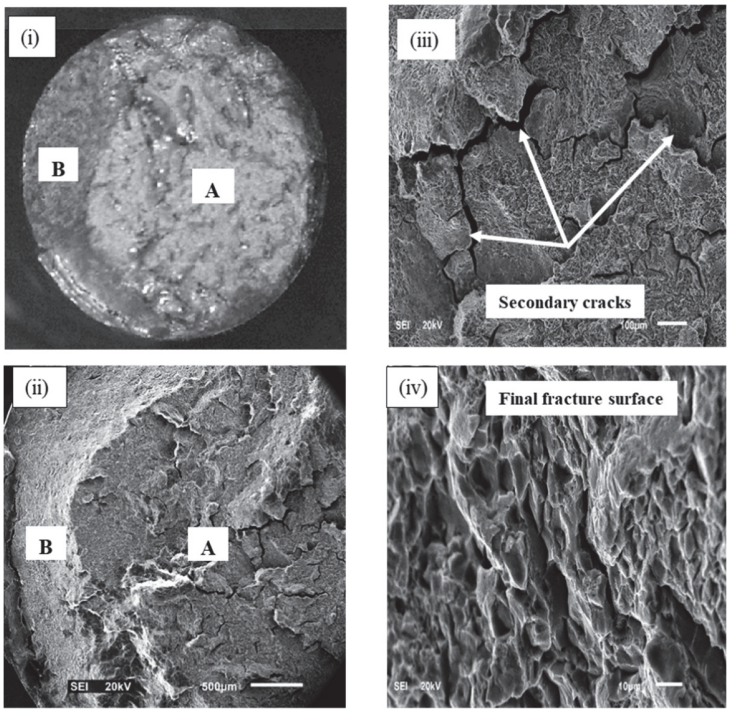

(c) Fractured surface of AW2099-T83 specimen tested at ε_a = 0.7%.

Figure 15: Fractography of fractured samples at selected strain amplitudes.

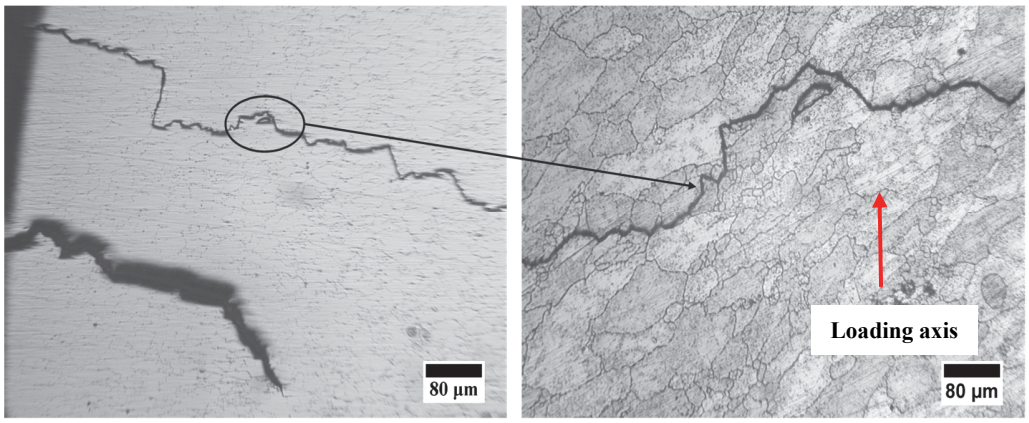

(a)

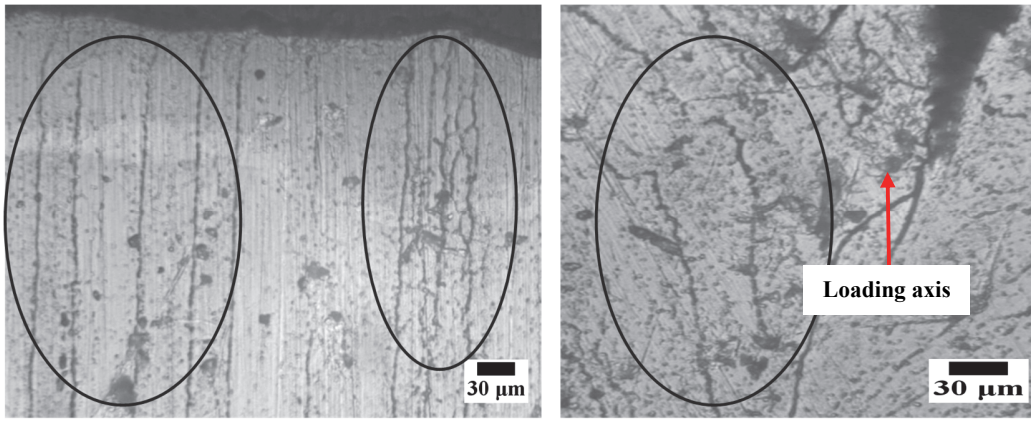

(b)

Figure 16: Optical micrographs of cracking mode.

CONCLUSIONS

The microstructure, monotonic tensile and axial strain-controlled fatigue behavior of AW2099 T83 have been studied. The grains present in the transverse orientation for the investigated aluminum-lithium alloy are a combination of small and large grains, while elongated primary grains with subgrains are present in the extrusion direction. Grains at the core are smaller than grains on the periphery in both transverse and extrusion directions leading to the conclusion that the microstructure is inhomogeneous. The grain sizes vary between 8 and 40 microns. Under static loading, the alloy exhibits low plastic deformation with very limited strain hardening. An ultimate strength of approximately 570 MPa was found for the alloy, which is comparable to most alloys of similar composition. However, the alloy possesses low ductility, which can be understood as the tradeoff for the high tensile strength.

Under strain-controlled fatigue, measureable plastic deformation for AW2099-T83 alloy was only present at highest applied strain amplitude of 0.7%. Below strain amplitude of 0.7%, the deformation was mainly elastic. The resistance to plastic deformation is due to the precipitate phases present in the alloy. The characteristic hysteresis loop evolution indicates that strain energy-based models cannot be used to describe the alloy in the present applied strain range. Cyclic axial stress evolution for AW2099-T83 alloy was found to be dependent both on the applied strain amplitude and on the number of cycles. Cyclic hardening was observed in the early loading cycles at all strain amplitudes. This is generally followed by stable hysteresis before starting to soften. Mean stress evolution for the alloy is generally low and compressive for strain amplitudes lower than 0.7%.

Through regression analysis, fatigue properties were determined and fitting curves were constructed to model strain-life curves for the alloy. Both Basquin and three-parameter equations were developed for the alloy with the latter resulting in a slightly better correlation for the fatigue data. The high fatigue strength coefficient exhibits by the alloy arises from its high monotonic strength which itself is derived from the strengthening precipitates present in the microstructure.

Stiffness and plastic strains were estimated through discrete analysis of hysteresis loops from which a trend for the damaging mechanism was profiled. It can be concluded that strain amplitude below 0.7% exhibits a damaging mechanism controlled by compressive strain, while above this strain amplitude, damage results from tensile plastic strain.

Fractographic analysis revealed that fracture characteristic is majorly by cleavage fracture and is semi-ductile in nature. Multiplication of secondary cracks along grain boundary was observed. The alloy is susceptible to fatigue crack along grain boundaries and through the grains. A post fracture metallography revealed that crack growth was mainly intergranular.

ACKNOWLEDGEMENT

This research is supported by a project grant KACST 230-34, from King AbdulAziz city for science and technology, Riyadh, Saudi Arabia. The authors would also like to acknowledge the support of King Fahd University of Petroleum & Minerals (KFUPM). The authors also acknowledge Westmoreland Mechanical Testing and Research Lab, UK for performing the tests.

REFERENCES

[1] Rioja, R.J., Liu, J. (2012). The evolution of Al-Li base products for aerospace and space applications, Metall. Mater. Trans. A Phys. Metall. Mater. Sci., 43A(9), pp. 3325–3337, DOI: 10.1007/s11661-012-1155-z.

[2] Wanhill, R.J.H. (1994). Status and prospects for aluminium-lithium alloys in aircraft structures, Fatigue, 16(1), pp. 3–20, DOI: 0142-1123/94/01/0003-18.

[3] Dursun, T., Soutis, C. (2014). Recent developments in advanced aircraft aluminium alloys, Mater. Des., 56, pp. 862–871.

[4] Eswara Prasad, N., Gokhale, A.A., Wanhill, R.J.H. (2014). Aluminum-Lithium Alloys: Processing, Properties, and Applications, Butterworth Heinemann.

[5] Bois-Brochu, A., Blais, C., Tchitembo Goma, F.A., Larouche, D. (2016). Modelling of anisotropy for Al-Li 2099 T83 extrusions and effect of precipitate density, Mater. Sci. Eng. A, 673, pp. 581–586, DOI: 10.1016/j.msea.2016.07.081.

[6] Li, J.-F., Liu, P., Chen, Y., Zhang, X., Zheng, Z. (2015). Microstructure and mechanical properties of Mg, Ag and Zn multi-microalloyed Al-(3.2-3.8)Cu-(1.0-1.4)Li alloys, Trans. Nonferrous Met. Soc. China, 25(2015), pp. 2103–2112.

[7] [7] Alexopoulos, N.D., Migklis, E., Stylianos, A., Myriounis, D.P. (2013). Fatigue behavior of the aeronautical Al – Li

(2198) aluminum alloy under constant amplitude loading, Int. J. Fatigue, 56, pp. 95–105.
[8] Srivatsan, T.S., Coyne, E.J. (1986). Cyclic stress response and deformation behaviour of precipitation-hardened aluminium-lithium alloys, Int. J. Fatigue, 4(8), pp. 201–208.
[9] Chen, X., Tromans, D. (1996). Short transverse fatigue crack propagation in 8090 Al-Li alloy: Re-ageing and environmental effects, Mater. Sci. Eng. A, 206(2), pp. 163–175, DOI: 10.1016/0921-5093(95)10008-3.
[10] Ohrloff, N., Gysler, a., Lütjering, G. (1987). Fatigue Crack Propagation Behavior of 2091 T8 and 2024 T3 Under Constant and Variable Amplitude Loading, Le J. Phys. Colloq., 48(C3), pp. c3-801-c3-807, DOI: 10.1051/jphyscol:1987394.
[11] Ranganathan, N., Adiwijayanto, F., Petit, J., Bailon, J.P. (1995). Fatigue crack propagation mechanisms in an aluminium lithium alloy, Acta Metall. Mater., 43(3), pp. 1029–1035.
[12] Wanhill, R.J.H., Bray, G.H. (2013). Fatigue crack growth behavior of aluminum-lithium alloys, Elsevier Inc.
[13] Akhtar, N., Wu, S.J. (2017). Macromechanics study of stable fatigue crack growth in Al-Cu-Li-Mg-Ag alloy, Fatigue Fract. Eng. Mater. Struct., 40, pp. 233–244.
[14] McMaster, F.J., Tabrett, C.P., Smith, D.J. (1998). Fatigue crack growth rates in Al-Li alloy 2090. Influence of orientation, sheet thickness and specimen geometry, Fatigue Fract. Eng. Mater. Struct., 21, pp. 139–150.
[15] Nicholls, D.J., Martin, J.W. (1990). Small crack growth in the aluminium–lithium alloys 8090 and 8091, Fatigue Fract. Eng. Mater. Struct., 13(1), pp. 83–94, DOI: 10.1111/j.1460-2695.1990.tb00578.x.
[16] Blankenship, C.P., Bray, G.H., Kaisand, L.R., Starke, E.A. (1995). Low cycle fatigue behavior of two Al-Li alloys, Fatigue Fract. Eng. Mater. Struct., 18(5), pp. 551–564.
[17] Liu, S.M., Wang, Z.G. (2003). Fatigue properties of 8090 Al-Li alloy processed by equal-channel angular pressing, Scr. Mater., 48(10), pp. 1421–1426, DOI: 10.1016/S1359-6462(03)00107-6.
[18] Jabra, J., Romios, M., Lai, J., Lee, E., Setiawan, M., Lee, E.W., Witters, J., Abourialy, N., Ogren, J.R., Clark, R., Oppenheim, T., Frazier, W.E., Es-Said, O.S. (2006). The Effect of Thermal Exposure on the Mechanical Properties of 2099-T6 Die Forgings, 2099-T83 Extrusions, 7075-T7651 Plate, 7085-T7452 Die Forgings, 7085-T7651 Plate, and 2397-T87 Plate Aluminum Alloys, J. Mater. Eng. Perform., 15(October), pp. 601–607, DOI: 10.1361/105994906X136142.
[19] Fu, B., Qin, G., Meng, X., Ji, Y., Zou, Y., Lei, Z. (2014). Microstructure and mechanical properties of newly developed aluminum – lithium alloy 2A97 welded by fiber laser, Mater. Sci. Eng. A, 617, pp. 1–11.
[20] Li, H., Huang, D., Kang, W., Liu, J., Ou, Y., Li, D. (2016). Effect of Different Aging Processes on the Microstructure and Mechanical Properties of a Novel Al – Cu – Li Alloy, J. Mater. Sci. Technol., 32, pp. 1049–1053.
[21] Lin, Y., Zheng, Z.Q., Li, S.C. (2014). Effect of solution treatment on microstructures and mechanical properties of 2099 Al–Li alloy, Arch. Civ. Mech. Eng., 14(1), pp. 61–71, DOI: 10.1016/j.acme.2013.07.005.
[22] Lin, Y., Zheng, Z., Li, S., Kong, X., Han, Y. (2013). Microstructures and properties of 2099 Al-Li alloy, Mater. Charact., 84, pp. 88–99, DOI: 10.1016/j.matchar.2013.07.015.
[23] Zhu, Z., Han, J., Gao, C., Liu, M., Song, J., Wang, Z., Li, H. (2017). Microstructures and mechanical properties of Al-Li 2198-T8 alloys processed by two different severe plastic deformation methods: A comparative study, Mater. Sci. Eng. A, 681(October), pp. 65–73, DOI: 10.1016/j.msea.2016.10.108.
[24] Jata, K. V., Starke, E.A. (1986). Fatigue Crack Growth and Fracture Toughness Behavior of an Al-Li-Cu Alloy, Metall. Trans. A, 17A(June), pp. 1011–1026.
[25] Alexopoulos, N.D., Proiou, A., Dietzel, W., Blawert, C., Heitmann, V., Zheludkevich, M., Kourkoulis, S.K. (2016). Mechanical properties degradation of (Al-Cu-Li) 2198 alloy due to corrosion exposure, Procedia Struct. Integr., 2, pp. 597–603, DOI: 10.1016/j.prostr.2016.06.077.
[26] Ma, Y.. E., Xia, Z.., Jiang, R.R., Li, W. (2013). Effect of welding parameters on mechanical and fatigue properties of friction stir welded 2198 T8 aluminum–lithium alloy joints, Eng. Fract. Mech., 114, pp. 1–11, DOI: 10.1007/s00170-015-7191-2.
[27] Cavaliere, P., De Santis, A., Panella, F., Squillace, A. (2009). Effect of anisotropy on fatigue properties of 2198 Al-Li plates joined by friction stir welding, Eng. Fail. Anal., 16(6), pp. 1856–65, DOI: 10.1016/j.engfailanal.2008.09.024.
[28] Adinoyi, M.J., Merah, N., Albinmousa, J. (2018). Shear fatigue behavior of AW2099-T83 aluminum-lithium alloy, Int. J. Fatigue, 117, pp. 101–110, DOI: 10.1016/j.ijfatigue.2018.07.028.
[29] ASTM E8/E8M-08, Standard Test Methods for Tension Testing of Metallic Materials, ASTM International, West Conshohocken, PA, 2008.
[30] ASTM International. (1999). Standard Practice for Strain-Controlled Fatigue Testing, E 606 -99, West Conshohocken, PA. 2004. 24.
[31] Bois-Brochu, A., Blais, C., Goma, F.A.T., Larouche, D., Boselli, J., Brochu, M. (2014). Characterization of Al–Li 2099

extrusions and the influence of fiber texture on the anisotropy of static mechanical properties, Mater. Sci. Eng. A, 597, pp. 62–69, DOI: 10.1016/j.msea.2013.12.060.
[32] Tchitembo Goma, F.A., Larouche, D., Bois-Brochu, A., Blais, C., Boselli, J., Brochu, M. (2014). Effect of extrusion aspect ratio and test temperatures on fatigue crack growth behavior of a 2099-T83 Al-Li alloy, Int. J. Fatigue, 59, pp. 244–253.
[33] Satya Prasad, K., Eswara Prasad, N., Gokhale, A.A. (2014).Microstructure and Precipitate Characteristics of Aluminum-Lithium Alloys. In: Eswara Prasad, N., Gokhale, A.A., Wanhill, R.J.H., (Eds.), Aluminum-Lithium Alloys: Processing, Properties, and Applications 1st ed., Elsevier Inc., pp. 99–137.
[34] Sun, Z., Huang, M. (2013). Fatigue crack propagation of new aluminum lithium alloy bonded with titanium alloy strap, Chinese J. Aeronaut., 26(3), pp. 601–605.
[35] Li, J.F., Liu, P.L., Chen, Y.L., Zhang, X.H., Zheng, Z.Q. (2015). Microstructure and mechanical properties of Mg, Ag and Zn multi-microalloyed Al-(3.2-3.8)Cu-(1.0-1.4)Li alloys, Trans. Nonferrous Met. Soc. China (English Ed., 25(7), pp. 2103–2112, DOI: 10.1016/S1003-6326(15)63821-3.
[36] Zheng, X., Luo, P., Chu, Z., Xu, J., Wang, F. (2018). Plastic flow behavior and microstructure characteristics of light-weight 2060 Al-Li alloy, Mater. Sci. Eng. A, 736, pp. 465–471, DOI: 10.1016/j.msea.2018.09.010.
[37] Eswara Prasad, N., Srivatsan, T.S., Wanhill, R.J.H., Malakondaiah, G., Kutumbarao, V.V. (2014).Fatigue Behavior of Aluminum–Lithium Alloys. In: Eswara Prasad, N., Gokhale, A.A., Wanhill, R.J.H., (Eds.), Aluminum-lithium Alloys 1st ed., Elsevier Inc., pp. 341–379.
[38] Branco, R., Costa, J.D., Antunes, F. V. (2012). Low-cycle fatigue behaviour of 34CrNiMo6 high strength steel, Theor. Appl. Fract. Mech., 58(1), pp. 28–34, DOI: 10.1016/j.tafmec.2012.02.004.
[39] Mughrabi, H. (2001). Fatigue Life and Cyclic Stress-Strain Behavior, Encycl. Mater., pp. 2917–2931.
[40] Stephens, Ralph, I., Fatemi, A., Stephens, Robert, R., Fuchs, Henry, O. (2001). Metal Fatigue in Engineering, 3, John Wiley & Sons.
[41] Suresh, S. (1998). Fatigue of Materials, Cambridge, Cambridge University Press.
[42] Gao, Z., Zhao, T., Wang, X., Jiang, Y. (2009). Multiaxial Fatigue of 16MnR Steel, J. Press. Vessel Technol., 131(2), pp. 021403, DOI: 10.1115/1.3008041.
[43] Szusta, J., Seweryn, A. (2017). Experimental study of the low-cycle fatigue life under multiaxial loading of aluminum alloy EN AW-2024-T3 at elevated temperatures, Int. J. Fatigue, 96, pp. 28–42, DOI: 10.1016/j.ijfatigue.2016.11.009.
[44] Borrego, L.P., Abreu, L.M., Costa, J.M., Ferreira, J.M. (2004). Analysis of low cycle fatigue in AlMgSi aluminium alloys, Eng. Fail. Anal., 11(5), pp. 715–725.
[45] Metal Handbook: Failure Analysis and Prevention (1986), Ohio, American Society for Metals.
[46] De-Feng, M., Guo-Qiu, H., Zheng-Fei, H., Zheng-Yu, Z., Cheng-Shu, C., Wei-Hua, Z. (2008). Crack initiation and propagation of cast A356 aluminum alloy under multi-axial cyclic loadings, Int. J. Fatigue, 30(10–11), pp. 1843–1850.

NOMENCLATURE AND ABBREVIATIONS

Al	aluminum
Al-Li	aluminum lithium
b	axial fatigue strength exponent
c	axial fatigue ductility exponent
CNC	computer numerical control
d	gage diameter of specimens
E	elastic modulus
E1	metallographic sample from edge of extrusion direction
E2	metallographic sample from midsection between the edge and center of extrusion direction
E3	metallographic sample from center of extrusion direction
E_s	residual stiffness
Exp	experimental
Freq	frequency
GPa	gigaPascal
K	monotonic tensile strength coefficient
kN	kiloNewton
mm	millimeter

MPa	megaPascal
n	monotonic tensile strain hardening exponent
N_f	fatigue life
ref	referenced
Spec	specimen
T1	metallographic sample from edge of transverse direction
T2	metallographic sample from midsection between the edge and center of transverse direction
T3	metallographic sample from center of transverse direction
α	primary grains in the extrusion direction
ε_a	axial strain amplitude
ε_e	axial elastic strain amplitude
$\boldsymbol{\varepsilon_f'}$	fatigue ductility coefficient
ε_p	axial plastic strain amplitude
σ_a	axial stress amplitude
$\boldsymbol{\sigma_f'}$	fatigue strength coefficient
σ_m	mean axial stress
σ_{max}	maximum axial stress
σ_{min}	minimum axial stress